A Standardized parameter-free algorithm for combined intravoxel incoherent motion and diffusion kurtosis analysis of diffusion imaging data

Wurnig, Moritz C ; Kenkel, David ; Filli, Lukas ; Boss, Andreas

Abstract: OBJECTIVES The aims of this study were to implement and systematically evaluate the performance of a new parameter-free segmented algorithm for analysis of diffusion imaging data using a combined intravoxel incoherent motion and diffusion kurtosis imaging (IVIM-DKI) model of spin diffusion in comparison with the simpler intravoxel incoherent motion (IVIM) model. MATERIALS AND METHODS A multistep algorithm was implemented intended to separate diffusion kurtosis from IVIM effects in multi-b-value diffusion measurements using an adaptive b-value threshold technique. For each possible b-value threshold (separating diffusion and perfusion effects), diffusion kurtosis analysis of high b-values is followed by IVIM analysis keeping kurtosis parameters fixed. The b-value threshold with smallest Akaike information criterion is chosen as best model solution. The algorithm was tested in diffusion data sets of the upper abdomen from 8 healthy volunteers with 16 different b-values and compared with a standard multistep IVIM analysis. RESULTS The proposed algorithm could successfully be applied to all data sets and provided a significantly better fit of the observed signal decay in all assessed organs (all $P < 0.03$). Using the proposed IVIM-DKI model of diffusion instead of an IVIM model had a systematic impact on the resulting IVIM parameters: The pure diffusion coefficient and the pseudodiffusion coefficient were significantly increased ($P < 0.03$ in all assessed organs), accompanied by a decrease in the perfusion fraction in liver, pancreas, renal cortex, and skeletal muscle (all $P < 0.02$). Optimal b-value thresholds separating diffusion from perfusion effects had a tendency to lower values when the IVIM-DKI model was used. CONCLUSIONS The proposed algorithm provides a new approach for separation of IVIM and kurtosis effects of diffusion data without organ-specific adaptation.

DOI: https://doi.org/10.1097/RLI.0000000000000223

Originally published at:
Wurnig, Moritz C; Kenkel, David; Filli, Lukas; Boss, Andreas (2016). A Standardized parameter-free algorithm for combined intravoxel incoherent motion and diffusion kurtosis analysis of diffusion imaging data. Investigative Radiology, 51(3):203-210.
DOI: https://doi.org/10.1097/RLI.0000000000000223

A Standardized Parameter-Free Algorithm for Combined Intravoxel Incoherent Motion and Diffusion Kurtosis Analysis of Diffusion Imaging Data

Moritz C. Wurnig, MD, MSc, David Kenkel, MD, Lukas Filli, MD, and Andreas Boss, MD, PhD

Objectives: The aims of this study were to implement and systematically evaluate the performance of a new parameter-free segmented algorithm for analysis of diffusion imaging data using a combined intravoxel incoherent motion and diffusion kurtosis imaging (IVIM-DKI) model of spin diffusion in comparison with the simpler intravoxel incoherent motion (IVIM) model.

Materials and Methods: A multistep algorithm was implemented intended to separate diffusion kurtosis from IVIM effects in multi-*b*-value diffusion measurements using an adaptive *b*-value threshold technique. For each possible *b*-value threshold (separating diffusion and perfusion effects), diffusion kurtosis analysis of high *b*-values is followed by IVIM analysis keeping kurtosis parameters fixed. The *b*-value threshold with smallest Akaike information criterion is chosen as best model solution. The algorithm was tested in diffusion data sets of the upper abdomen from 8 healthy volunteers with 16 different *b*-values and compared with a standard multistep IVIM analysis.

Results: The proposed algorithm could successfully be applied to all data sets and provided a significantly better fit of the observed signal decay in all assessed organs (all $P < 0.03$). Using the proposed IVIM-DKI model of diffusion instead of an IVIM model had a systematic impact on the resulting IVIM parameters: The pure diffusion coefficient and the pseudodiffusion coefficient were significantly increased ($P < 0.03$ in all assessed organs), accompanied by a decrease in the perfusion fraction in liver, pancreas, renal cortex, and skeletal muscle (all $P < 0.02$). Optimal *b*-value thresholds separating diffusion from perfusion effects had a tendency to lower values when the IVIM-DKI model was used.

Conclusions: The proposed algorithm provides a new approach for separation of IVIM and kurtosis effects of diffusion data without organ-specific adaptation.

Key Words: intravoxel incoherent motion, diffusion-weighted imaging, diffusion kurtosis imaging, magnetic resonance, pseudodiffusion

(*Invest Radiol* 2015;00: 00–00)

Diffusion weighted imaging (DWI) is a well-established clinical tool today. Although it is known that diffusion weighting and signal intensity in DWI is dependent on the chosen *b*-value modeling of diffusion in perfused biological tissues remains challenging. Several different models for the signal decay in dependence on used *b*-values in DWI have been proposed. These include the classical monoexponential model of passive water diffusivity, and the intravoxel incoherent motion (IVIM) model[1] including the contribution of perfusion effects present at low *b*-values. Furthermore, the diffusion kurtosis (DKI) model was proposed, which takes into account the non-Gaussian diffusion behavior of water molecules at high *b*-values.[2]

Because the IVIM model and the DKI model cover different aspects of diffusion, a combined IVIM-DKI model might describe diffusion in perfused biological tissues more accurately. However, as diffusion models are getting more complex, fitting of the measured signal decay becomes increasingly unstable with higher number of free parameters because of underdetermination, which is especially true for the IVIM model, a fact that greatly hampered the usage of these more complex models. Another fact adding to the instability of typically used algorithms to fit the whole IVIM model at once is the dependence of the fitting variables among each other.[3] To overcome this issue, different approaches have been used, including fixing of the pseudodiffusion coefficient, Bayesian fitting, and discretization of the fitting parameters.[4–10] One of the most commonly used approaches today is a multistep procedure calculating separately 1 IVIM parameter after the other,[11–23] thereby reducing the degree of freedom for each individual step.

Still, this method needs the definition of an arbitrary *b*-value threshold above which perfusion effects are expected to be negligible, which has been shown to influence the calculated IVIM parameters. To eliminate the need of choosing such a *b*-value threshold, a parameter-free version of the very commonly used multistep procedure for the IVIM model was proposed recently.[3] In this study, we expanded the proposed parameter-free segmented algorithm for a combined IVIM-DKI model of diffusion and evaluated its performance and possible systematic differences in comparison with the simpler IVIM diffusion model.

MATERIALS AND METHODS

Subjects

Eight healthy subjects (6 men, 2 women; median age, 26 years, range, 23–39 years) were prospectively included in this study. Written informed consent was obtained from all subjects and the study was approved by the local ethical review committee.

Imaging Protocol

For magnetic resonance imaging, a 3 T whole-body magnetic resonance scanner (Ingenia, Philips, Best, the Netherlands) with a 16-channel flexible anterior phased-array coil and built-in posterior coil was used. A spin-echo prepared echo-planar imaging sequence was used to acquire diffusion weighted image data sets of the upper abdomen in axial sections using trace weighting. For the acquisition, 16 *b*-values (0, 10, 20, 40, 90, 100, 170, 200, 210, 240, 390, 530, 620, 750, 970, and 1000 s/mm^2) were chosen as suggested by Lemke et al.[24] Additional sequence parameters included the following: repetition time, 5000 milliseconds; echo time, 69 milliseconds; matrix size, 144 × 144; in-plane resolution, 2.8 × 2.8 mm; slice thickness, 5 mm; number of averages, 6; parallel imaging SENSE factor, 2; spectral selection attenuated inversion recovery fat suppression; and receiver bandwidth, 2321 Hz/px. Total scan time was 46 minutes 10 seconds. All imaging was performed during free breathing.

Region of Interest Definition

To acquire signal-intensity curves as a function of the *b*-value, a region of interest (ROI) analysis was performed similar to Wurnig et al.[3] All ROIs were defined using institutional computer scripts written in the programming language Matlab (The MathWorks, Natick, MA).

Received for publication July 1, 2015; and accepted for publication, after revision, September 17, 2015.
From the Department of Diagnostic and Interventional Radiology, University Hospital Zurich, Switzerland.
Conflicts of interest and sources of funding: none declared.
Correspondence to: Moritz C. Wurnig, MD, MSc, Department of Diagnostic and Interventional Radiology, University Hospital Zurich, Ramistrasse 100, CH-8091 Zurich, Switzerland. E-mail: moritz.wurnig@usz.ch.

ISSN: 0020-9996/15/0000–0000
DOI: 10.1097/RLI.0000000000000223

Polygonal ROIs were defined on the $b = 0$ s/mm^2 image and subsequently copied to all other b-value images of the same data set. To exclude contributions from macroscopic vascular flow, large vessels were avoided in the manual ROI definitions. The following body regions were assessed: liver (left and right lobe separately), pancreas, spleen, kidney (cortex and medulla separately), and erector spinae muscle. Standardized ROI definitions were used as specific anatomical regions were defined for placement. Regions of interest were drawn in liver segment III (left liver lobe) and liver segment V/VI (right liver lobe). For the pancreas, the ROI was placed in the middle of the cauda in the slice containing its largest part. The definition of the ROI in the spleen was performed in the middle of the spleen in the slice covering the hilus. For the kidney, ROIs were defined in the right kidney in the slice covering the hilus (cortex and medulla). Finally, an ROI was placed in the middle of the left erector spinae muscle in the slice at the level of the renal arteries. Figure 1 shows typical ROI definitions as described. All signal intensity curves were normalized to a maximum of 1 for the $b = 0$ s/mm^2 image.

Combined IVIM-DKI Analysis

In the standard IVIM model, the signal intensity curves from a DWI experiment with multiple b-values are divided in a part dominated by diffusion effects and in a part dominated by perfusion effects, as described by

$$S_b/S_0 = F_p \exp(-bD^*) + \left(1-F_p\right) \exp(-bD). \quad (1)$$

In this equation S_b represents the signal intensity in the DWI data acquired with the b-value, S_0 is the signal intensity in the $b = 0$ s/mm^2 image, F_p is the perfusion fraction, D^* is the pseudodiffusion coefficient, and D is the diffusion coefficient of "pure" molecular water diffusion. Although this model provides a more realistic description of the signal behavior of perfused tissue in diffusion experiments, it still lacks some potentially important components as it is known that "pure" diffusion can be further subdivided in fast- and slow-diffusing components. A well-known model for the description of this phenomenon is the diffusion kurtosis model, which introduces the kurtosis—an indicator for the non-Gaussianity of the diffusion. In the present study, we combined the IVIM and the DKI model to describe the tissue signal intensity curves from DWI experiments more precisely by using the following equation:

$$S_b/S_0 = F_p \exp(-bD^*) + \left(1-F_p\right) \exp\left(-bD + \frac{K}{6} b^2D^2\right). \quad (2)$$

In this equation, the parameter K (the kurtosis) is a measure for the non-Gaussianity of the diffusion dominated part of the observed signal decay in DWI experiments.

To compute IVIM parameters from Eq. (1) typically a multistep approach is used,[11–19] where D is calculated from all b-value above a threshold, where perfusion contributions are presumed to be negligible. Subsequently, F_p is calculated from the y-axis intercept of "pure" diffusion and finally D^* in separate steps. To overcome the need of choice of an appropriate threshold (which also might be influenced by the assessed organ, age, and the presence of disease), recently, a parameter-free algorithm was introduced.[3] Here, we extended the proposed algorithm for a combined IVIM-DKI analysis using Eq. (2).

In the first step of the algorithm, parameters D and K are calculated using a fit to the log-transformed signal intensities of the data acquired with the n highest b-values:

$$\log S_b = -bD + \frac{K}{6} b^2D^2 + \log S_0'. \quad (3)$$

Then F_p is calculated from the measured signal intensity in the $b = 0$ s/mm^2 image S_0 and the calculated signal intensity S_0' as follows:

$$F_p = \frac{S_0 - S_0'}{S_0} \quad (4)$$

In the final step, a nonlinear fit is used to fit the signal intensities from all b-values to the complete equation,[2] with the only variable parameter D^* using the calculated and fixed values for D, K, and F_p. For all fits,

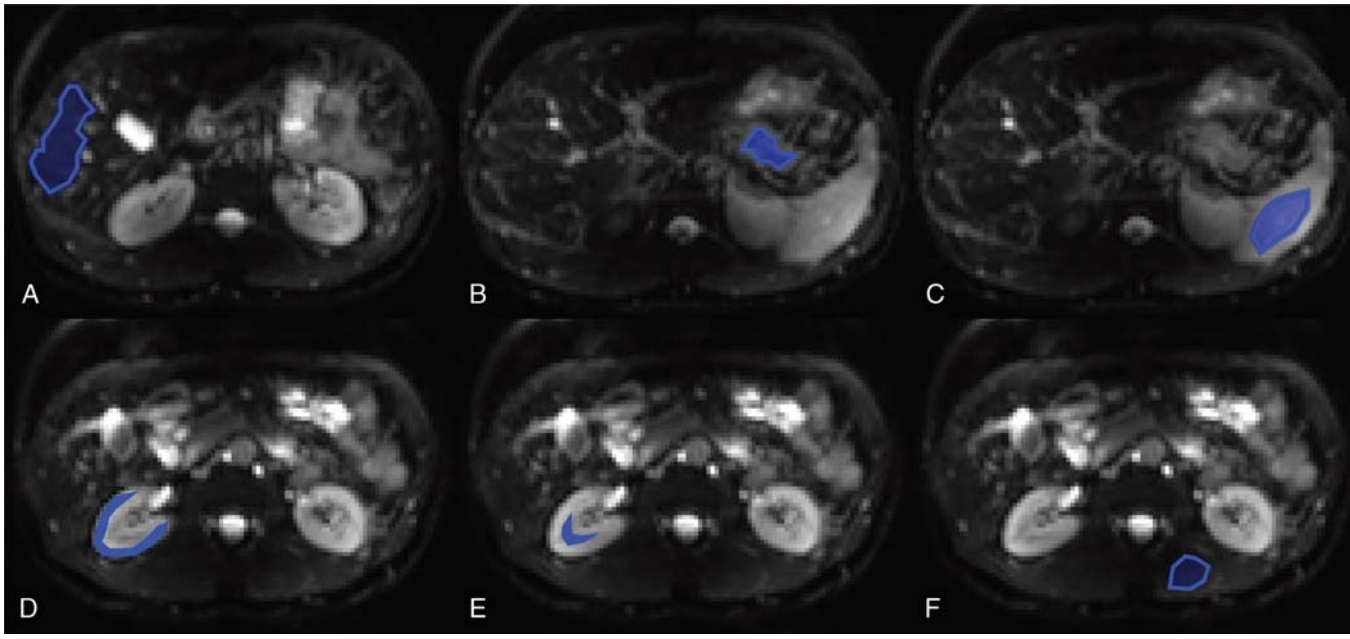

FIGURE 1. Typical region of interest placement for (A) right liver lobe, (B) pancreas, (C) spleen, (D) kidney cortex, (E) kidney medulla, and (F) erector spinae muscle.

an algorithm based on the Levenberg-Marquardt technique was used, which also calculates the sum of the squared residuals. To find the optimal *b*-value threshold, the above described procedure is performed in a loop using the highest n *b*-values (n ranging from *N* to 3, *N* being the number of all available *b*-values), which are applied for the calculation of *D*, *K*, and F_p, whereas the subsequent IVIM-DKI fit is kept with all *b*-values. Finally, the best fitting curve is determined for all $N - 2$ evaluations. The above described algorithm is depicted as a flow chart in Figure 2.

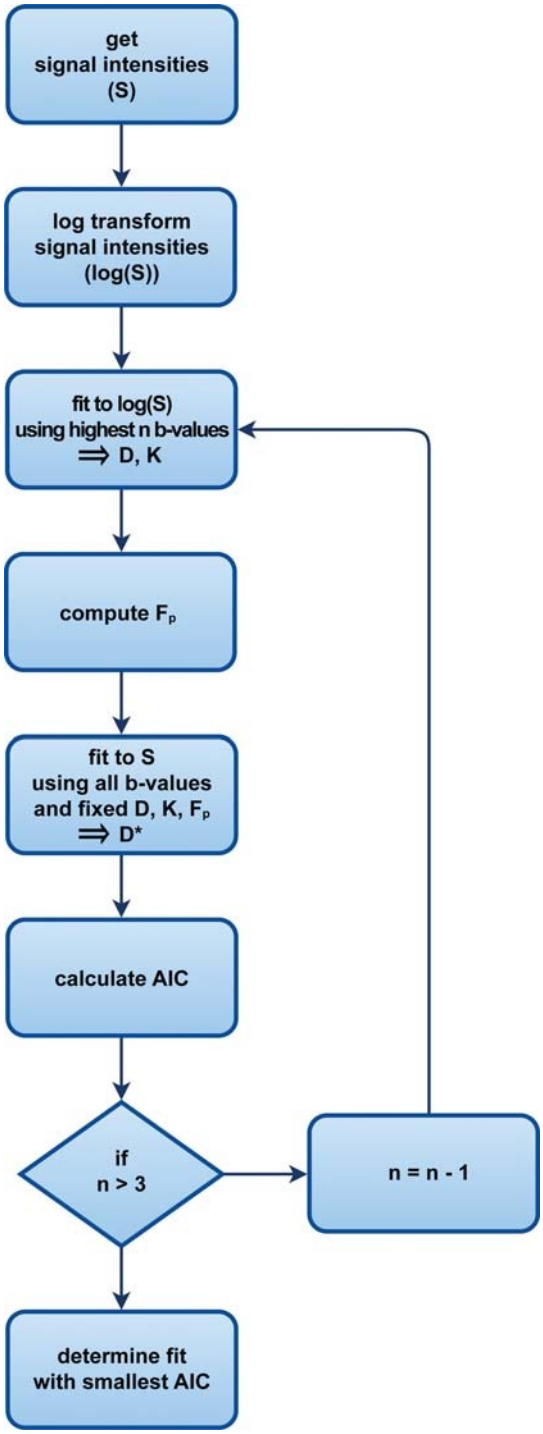

FIGURE 2. Flowchart of the proposed algorithm for the combined intravoxel incoherent motion and diffusion kurtosis imaging analysis of diffusion imaging data. The Akaike information criterion (AIC) value is computed in a loop while decreasing the number of *b*-values used for the computation of *D* and *K* from *N* (all *b*-values) to 3 (and therefore decreasing the used *b*-value threshold). Finally, the fit with the smallest AIC is determined.

To determine the best fitting-curve (using all *b*-value data, but different *b*-value thresholds), Akaike's information criterion (AIC) was used, which rewards lower error residuals but penalizes the number of fitting parameters. With the assumption of normally distributed residuals of the fit, the AIC can be determined according to

$$AIC = N \log \sigma^2 + 2k, \quad (5)$$

Here, *N* denotes the number of fitting points (fixed and equal to number of all available *b*-values), σ^2 is the variance of the residuals, and *k* is the number of fitting parameters. Note that *k* is fixed for the used model of diffusion and has no effect on the determined *b*-value threshold or on the fitted parameters. Lower AIC values correspond to better fitting curves. The rationale to use the AIC instead for instance minimizing the sum of the squared residuals was that using a more complex model of diffusion such as IVIM-DKI (using more free parameters) could lead to overfitting of the data. Such overfitting is penalized by the AIC but not by the sum of the squared residual.

Statistical Evaluation

The optimal *b*-value thresholds leading to the best fitting curves were determined for each subject and organ using the previously described parameter-free IVIM algorithm as well as the extended IVIM-DKI version. For each organ, mean values and standard deviations were computed for IVIM and DKI parameters (and resulting AIC values). To test for differences between the IVIM algorithm and the DKI-IVIM algorithm, paired Student *t* tests were used for the resulting IVIM and DKI parameters as well as the resulting AIC values. To test for differences between the automatically chosen *b*-value thresholds, Wilcoxon signed-rank tests were used. All *P* values < 0.05 were considered to be statistically significant. All statistical analyses were performed by using commercially available software (GraphPad Prism version 5.04 for Windows, GraphPad Software, La Jolla, CA, USA).

RESULTS

Both algorithms could be successfully applied to all data sets, meaning that in the ROI analysis for each volunteer and organ a minimum of the AIC criterion was reached defining the *b*-value threshold. Parametrical maps for all free parameters of the evaluated diffusion models could be obtained in appropriate image quality (cp. Fig. 3). Typical fitting curves for liver parenchyma and renal cortex are provided in Figure 4 for both algorithms. In general, visually, a better fitting curve was noted when the IVIM-DKI algorithm was used (Fig. 4). Furthermore, a tendency to choose lower optimal *b*-value thresholds for the separation of perfusion and diffusion effects of the IVIM-DKI algorithm was observed, especially in the kidney (cortex and medulla) and muscle tissue (Table 1, Figs. 3 and 5). However, statistically significant differences for the choice of optimal *b*-value thresholds between the algorithms were found only in the kidney cortex ($P = 0.008$).

Mean *D* values as well as mean *D** values significantly increased in all assessed organs when using the IVIM-DKI model ($P < 0.03$ for all comparisons), whereas F_p values significantly decreased in the liver (left and right lobe), the pancreas, the renal medulla, and erector spinae muscle. These differences were accompanied by a significant decrease in the AIC—indicating a better-fitting curve—in all assessed organs when the IVIM-DKI model was used (cp. Figs. 4 and 6). The typical behavior of the AIC for different thresholds is depicted in Figure 5 for both the IVIM and IVIM-DKI models.

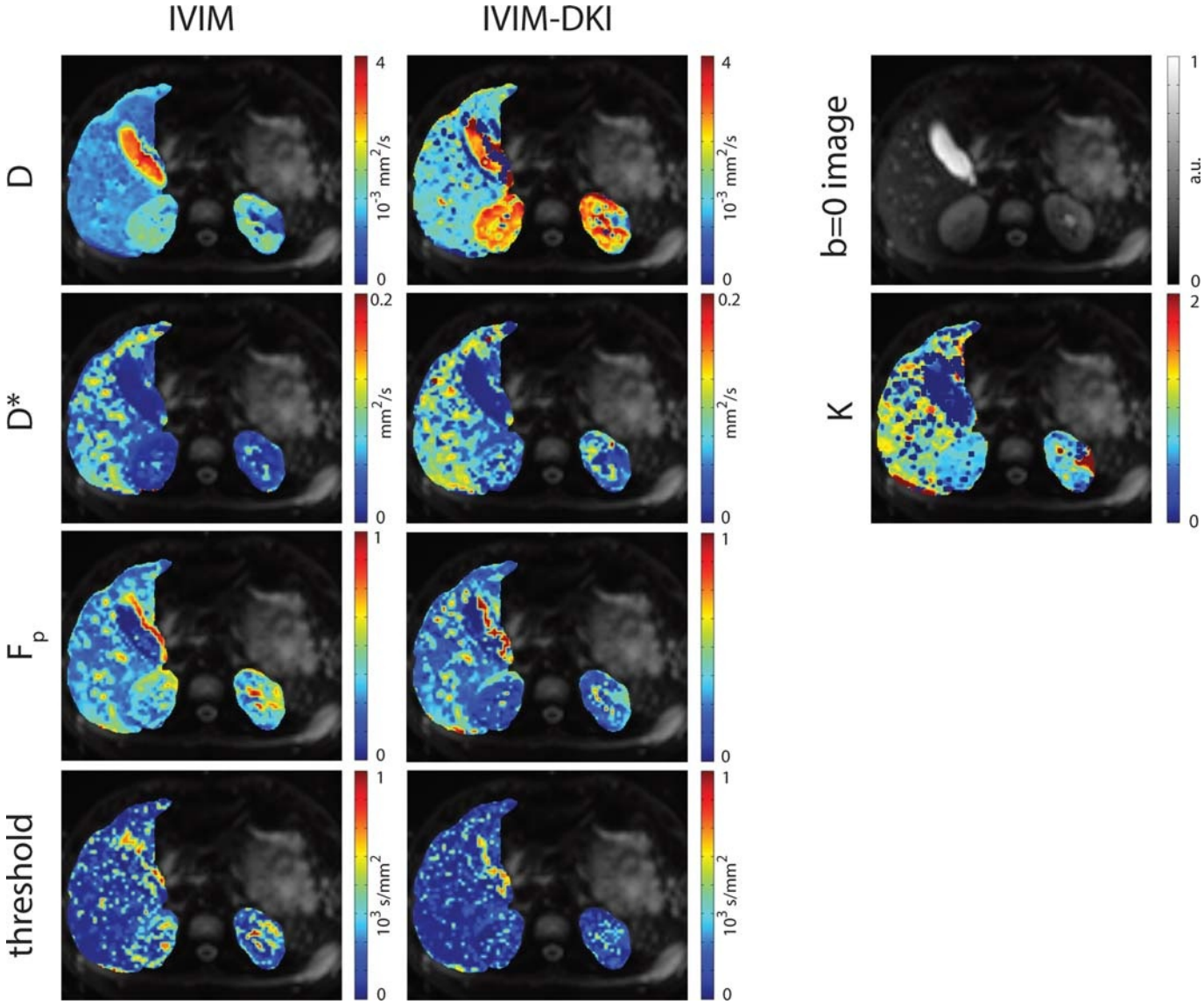

FIGURE 3. Parametrical maps of pixel-wise intravoxel incoherent motion (IVIM) and combined IVIM and diffusion kurtosis imaging (IVIM-DKI) curve computation. The pixel-wise computation of the curves is more demanding compared with region of interest analysis; therefore, noise contribution is higher. However, several aspects can be appreciated: (1) The consideration of the diffusion kurtosis results in increased true diffusion *D*, for instance in the liver. (2) Accordingly F_p is decreased, most prominent in the renal cortex. (3) Furthermore, an increase in *D** can be noted when the IVIM-DKI model is used. (4) In general, optimal *b*-value thresholds tend to lower values when kurtosis is considered. (5) Kurtosis is higher in the liver compared with renal tissue. (6) Kurtosis is zero in fluid collections such as the gall bladder. High F_p is seen at the margin of the gallbladder because of motion artifacts.

When using the IVIM-DKI algorithm, the typical characteristics of the assessed organs did not change: Liver and pancreas showed the highest values for perfusion fraction F_p and the pseudodiffusion coefficient *D**. Liver exhibited the typical difference between the left and right lobes, probably because of motion (breathing, cardiac) as well as susceptibility effects resulting from the stomach. The spleen demonstrated the lowest *D* values as well as a low perfusion fraction while *D** was high. In the kidneys, the highest *D* values in combination with the lowest *D** values were observed. Muscle tissue showed *D* values comparable with that in pancreas, a very low perfusion fraction, and low *D** values (cp. Fig. 6).

Kurtosis showed the following behavior: Whereas liver had the highest *K* values (left: 1.55 ± 0.73; right, 1.50 ± 0.46), followed by spleen (1.09 ± 0.36) and pancreas (0.91 ± 0.21), muscle tissue (0.58 ± 0.19) and kidney showed the lowest values (cortex: 0.65 ± 0.08; medulla: 0.45 ± 0.34).

DISCUSSION

In this study, we propose a new standardized parameter-free algorithm for combined IVIM-DKI analysis of diffusion imaging data and investigated the influence of the consideration of non-Gaussian diffusion in the IVIM model of diffusion on the derived parameters. To this end, we modified the recently proposed parameter-free segmented algorithm[3] to allow for calculation of the parameters of a combined IVIM-DKI model. We could show that the inclusion of kurtosis in the well-established IVIM model of diffusion has several effects: First, curve fitting to the signal decay is improved, thereby potentially

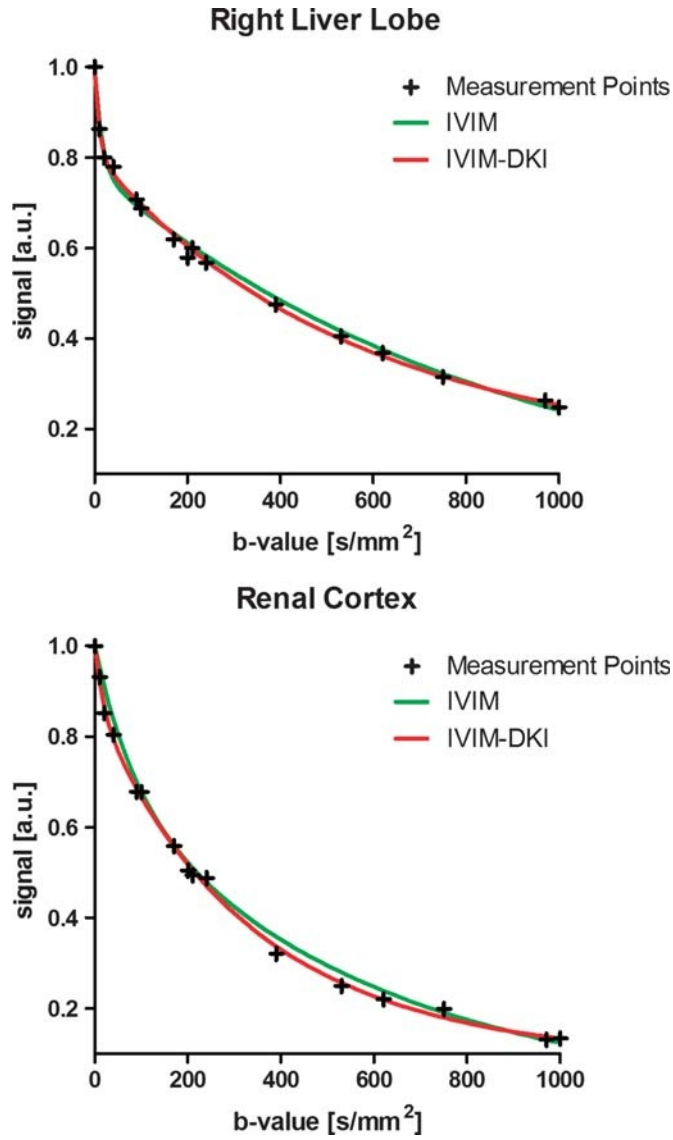

FIGURE 4. Typical wise intravoxel incoherent motion (IVIM) and combined IVIM and diffusion kurtosis imaging (IVIM-DKI) fitting curves are shown for liver and kidney parenchyma. The combined IVIM-DKI approach results in an improved description of the measurement points with smaller residuals and a lower Akaike information criterion (AIC) value (right liver: $AIC_{ivim} = -130.1$, $AIC_{ivim\text{-}dki} = -142.7$; renal cortex: $AIC_{ivim} = -123.1$, $AIC_{ivim\text{-}dki} = -136.4$). The consideration of the diffusion kurtosis in the fit causes an increase in the true diffusion D (right liver: $D_{ivim} = 1.16 \times 10^{-3}$ mm^2/s, $D_{ivim\text{-}dki} = 1.53 \times 10^{-3}$ mm^2/s; renal cortex: $D_{ivim} = 1.72 \times 10^{-3}$ mm^2/s, $D_{ivim\text{-}dki} = 2.80 \times 10^{-3}$ mm^2/s) and the pseudodiffusion D^* (right liver: $D^*_{ivim} = 65.5 \times 10^{-3}$ mm^2/s, $D^*_{ivim\text{-}dki} = 103.3 \times 10^{-3}$ mm^2/s; renal cortex: $D^*_{ivim} = 11.8 \times 10^{-3}$ mm^2/s, $D^*_{ivim\text{-}dki} = 56.3 \times 10^{-3}$ mm^2/s) compared with the simpler IVIM model, whereas F_p (right liver: $F_{pivim} = 0.229$, $F_{pivim\text{-}dki} = 0.192$; renal cortex: $F_{pivim} = 0.303$, $F_{pivim\text{-}dki} = 0.125$) is decreased. Although the same b-value threshold (20 s/mm^2) is chosen in the right liver lobe for the IVIM and the IVIM-DKI model, the threshold in the renal cortex was lower when the IVIM-DKI model was used ($threshold_{ivim} = 170$ s/mm^2, $threshold_{ivim\text{-}dki} = 40$ s/mm^2).

improving the informative value of the calculated parameters. Second, the true diffusion coefficient D as well as the pseudodiffusion coefficient D^* increase accompanied by a decrease in the perfusion fraction F_p. Third, the optimal b-value threshold for curve fitting tends to decrease, although significance was reached only for the kidney cortex. Fourth, all organs showed a positive kurtosis.

Although previous studies have investigated which diffusion model fits best for the description of perfused biological tissues, to our knowledge, only 1 of these studies included the IVIM-DKI model,[25] whereas most other studies investigated IVIM and DKI separately.[26–28] As both models, IVIM and DKI, were usually among the best-fitting models and the covered aspects of both models are complementary, combining both models seems a logical next step. Still, a systematic analysis of possible systematic changes when combining the models was not conducted, as the study by Lu et al.[25] focused on other aspects.

It has been previously described that introducing kurtosis in the monoexponential diffusion model systematically increases the observed diffusion coefficient,[29,30] which is in line with the findings in our study when kurtosis was introduced in the IVIM model. For positive kurtosis, such as observed in our study as well as in other dedicated DKI studies,[2,30–33] at least a part of this effect can be explained with the way kurtosis is introduced in the model, as D and K are introduced in the equation with opposite signs.

TABLE 1. Comparison of Optimal *b*-Value Thresholds Between IVIM and IVIM-DKI

	Optimal *b*-Value Threshold IVIM			Optimal *b*-Value Threshold IVIM-DKI			
	First Quartile	Median	Third Quartile	First Quartile	Median	Third Quartile	*P*
Left liver lobe	20	40	40	20	40	40	1.000
Right liver lobe	20	20	20	20	40	40	0.089
Pancreas	10	20	20	12.5	20	77.5	0.198
Renal medulla	10	60	495	10	20	77.5	0.246
Renal cortex	117.5	170	192.5	10	25	77.5	0.008
Spleen	10	20	40	12.5	20	40	0.854
Erector spinae muscle	12.5	245	597.5	10	10	72.5	0.063

IVIM indicates intravoxel incoherent motion; DKI, diffusion kurtosis imaging.

When compared with the literature, the measured values for the kurtosis differed from the values reported in dedicated DKI studies: Whereas in the liver higher values were found (this study, right liver lobe: $K = 1.50 \pm 0.46$; Filli et al,[31] right liver lobe: 1.04 ± 0.25), values in the spleen were lower (this study: $K = 1.09 \pm 0.36$; Filli et al[31]: 1.72 ± 0.32). *K* values in the kidneys were within the range reported in the literature (medulla: $K = 0.56$–0.79; cortex: $K = 0.56$–0.94[31,34,35]). These differences indicate that including the kurtosis in the IVIM model not only has an effect on the derived IVIM parameters but also affects the measured kurtosis. However, it cannot be ruled out that the observed kurtosis is also partly affected by the background noise floor and the lower signal-to-noise ratio at higher *b*-values. On the other hand deriving the kurtosis within an IVIM-DKI model might have introduced additional variation of *K*, when compared with studies using DKI alone.

An interesting observed effect was the tendency of the IVIM-DKI algorithm to choose lower optimal *b*-value thresholds in comparison with the IVIM algorithm. A reason for this may lie in the interdependence of the *b*-value threshold and the true diffusion coefficient *D*,[3] which in turn is dependent on the kurtosis *K* in the IVIM-DKI approach. More specific, this may indicate that the nonconsideration of the kurtosis may lead to a bias in IVIM fitting of DWI data.

These findings illustrate important aspects in the description of diffusion data with advanced models such as IVIM, DKI, or IVIM-DKI, namely, the interpretation of the obtained parameters as potential biomarkers. The principle aspects in the establishment of diffusion models may be summarized to the following:

a. More complex models require a higher number of parameters, which need to be determined with sufficient stability from a limited number of *b*-value measurements using sophisticated mathematical fitting algorithms.
b. The parameters are not independent but are interdependent in a highly complex relationship. This interdependence cannot be reflected by 1 single describing equation, as it reflects physiological and physical properties.

Typical physical and physiological properties of perfused biological tissues as assessed with the IVIM-DKI model are as follows:

a. For all tissues, a specific *b*-value threshold can be determined. Diffusion data acquired with *b*-values higher than this threshold include minor to negligible contributions from perfusion effects.
b. The kurtosis *K* generally has a positive value.

In our multistep algorithm, we tried to optimize the stability of the parameters by a step-wise computation of the respective parameters, whenever possible, keeping the simultaneously acquired parameters as low as possible (only *D* and *K* are fitted within the same computation step). In both models, the described IVIM and the IVIM-DKI

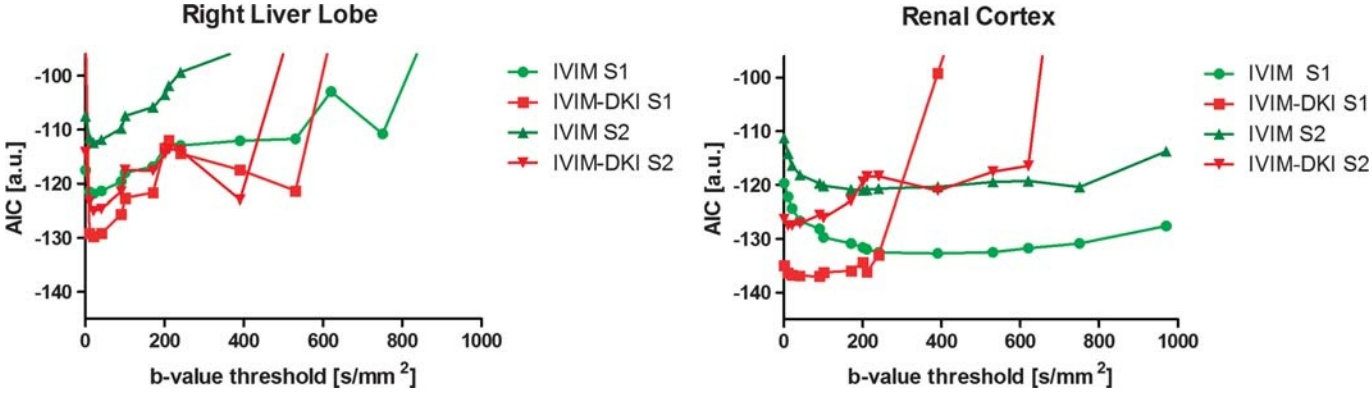

FIGURE 5. Typical behavior of the Akaike information criterion (AIC) for different thresholds for both the intravoxel incoherent motion (IVIM) and combined IVIM and diffusion kurtosis imaging (IVIM-DKI) diffusion models in 2 subjects (S1 and S2). Note whereas for liver tissue, both models show the same characteristics with reaching the *b*-value threshold with the lowest AIC already at very low *b*-values followed by a steady increase in the AIC for higher *b*-values, in the kidney, optimal *b*-value thresholds for the IVIM-DKI model are lower than for the IVIM model.

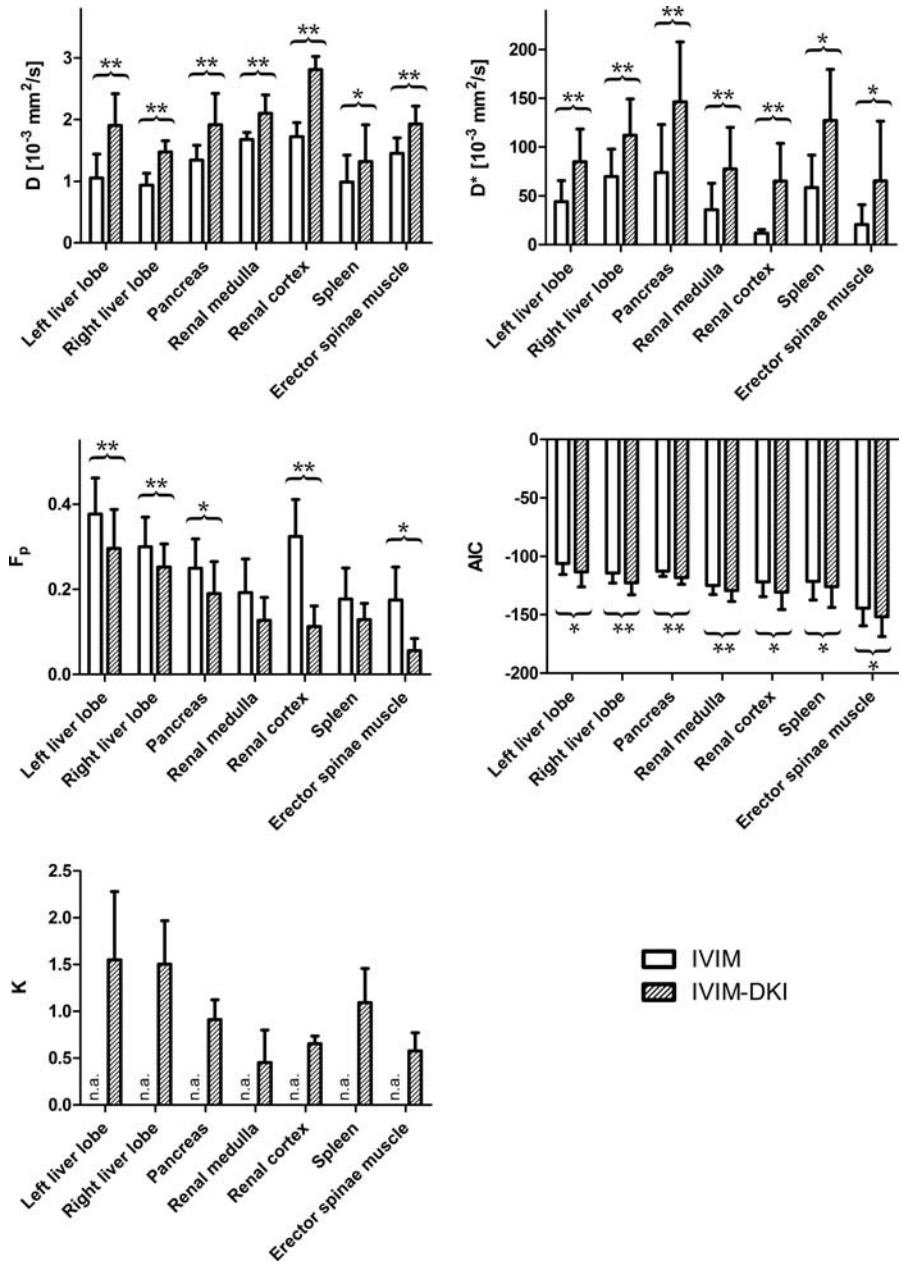

FIGURE 6. Comparison of parameters of the intravoxel incoherent motion (IVIM) and combined IVIM and diffusion kurtosis imaging (IVIM-DKI) models. Mean and standard deviations for the region of interest (ROI) analysis over all subjects are shown. Statistical significances with $P < 0.05$ are marked with *, significances with $P < 0.01$ are marked with **.

algorithms, the best *b*-value threshold is chosen by minimizing AIC. The significantly better fit of the IVIM-DKI model may indicate that the resulting parameters, with their systematic deviation (in comparison with the IVIM model), might describe diffusion in perfused biological tissues more accurately.

The following limitations for our study apply: First, the number of assessed volunteers was limited. Second, as triggering was not an option due to time constraints, breathing motion might have added variability to the results, although subjects were asked to breathe gently and periodically. Third, as for the original parameter-free algorithm for IVIM analysis, there is a remaining dependence of the results on the chosen and acquired *b*-values for the new proposed IVIM-DKI algorithm also, because only these *b*-values can be considered by the algorithm in terms of a possible threshold. Fourth, the introduction of additional parameters in the IVIM-DKI model might have an influence on the reproducibility of the derived parameters. This issue needs to be addressed in a dedicated reproducibility study. Fifth, the chosen highest *b*-value might have influenced the resulting kurtosis as the curvature of the observed signal decay might be incomplete. However, studies on DKI in the abdomen usually have used lower maximum *b*-values when compared with the present study.[31,34,35] Furthermore, the rather long acquisition time of the chosen approach limits its usage for clinical applications.

In conclusion, we demonstrated that the proposed parameter-free algorithm for IVIM-DKI analysis provides a new approach for separation of IVIM and kurtosis effects of diffusion data without organ-specific

adaptation. While the introduction of kurtosis in the IVIM model of diffusion leads to alterations of the resulting IVIM parameters, a significantly better fitting of the measured signal decay curves in diffusion experiments in perfused biological tissues can be obtained compared with a conventional multistep IVIM approach.

REFERENCES

1. Le Bihan D, Breton E, Lallemand D, et al. MR imaging of intravoxel incoherent motions: application to diffusion and perfusion in neurologic disorders. *Radiology*. 1986;161:401–407.
2. Jensen JH, Helpern JA, Ramani A, et al. Diffusional kurtosis imaging: the quantification of non-Gaussian water diffusion by means of magnetic resonance imaging. *Magn Reson Med*. 2005;53:1432–1440.
3. Wurnig MC, Donati OF, Ulbrich E, et al. Systematic analysis of the intravoxel incoherent motion threshold separating perfusion and diffusion effects: proposal of a standardized algorithm. *Magn Reson Med*. 2014. [Epub ahead of print].
4. Dyvorne HA, Galea N, Nevers T, et al. Diffusion-weighted imaging of the liver with multiple *b* values: effect of diffusion gradient polarity and breathing acquisition on image quality and intravoxel incoherent motion parameters—a pilot study. *Radiology*. 2013;266:920–929.
5. Neil JJ, Bretthorst GL. On the use of Bayesian probability theory for analysis of exponential decay data: an example taken from intravoxel incoherent motion experiments. *Magn Reson Med*. 1993;29:642–647.
6. Rheinheimer S, Stieltjes B, Schneider F, et al. Investigation of renal lesions by diffusion-weighted magnetic resonance imaging applying intravoxel incoherent motion-derived parameters—initial experience. *Eur J Radiol*. 2012;81:e310–e316.
7. Doblas S, Wagner M, Leitao HS, et al. Determination of malignancy and characterization of hepatic tumor type with diffusion-weighted magnetic resonance imaging: comparison of apparent diffusion coefficient and intravoxel incoherent motion-derived measurements. *Invest Radiol*. 2013;48:722–728.
8. Iima M, Yano K, Kataoka M, et al. Quantitative non-Gaussian diffusion and intravoxel incoherent motion magnetic resonance imaging: differentiation of malignant and benign breast lesions. *Invest Radiol*. 2015;50:205–211.
9. Klauss M, Lemke A, Grünberg K, et al. Intravoxel incoherent motion MRI for the differentiation between mass forming chronic pancreatitis and pancreatic carcinoma. *Invest Radiol*. 2011;46:57–63.
10. Lemke A, Laun FB, Klauss M, et al. Differentiation of pancreas carcinoma from healthy pancreatic tissue using multiple *b*-values: comparison of apparent diffusion coefficient and intravoxel incoherent motion derived parameters. *Invest Radiol*. 2009;44:769–775.
11. Callot V, Bennett E, Decking UK, et al. In vivo study of microcirculation in canine myocardium using the IVIM method. *Magn Reson Med*. 2003;50:531–540.
12. Cohen AD, Schieke MC, Hohenwalter MD, et al. The effect of low *b*-values on the intravoxel incoherent motion derived pseudodiffusion parameter in liver. *Magn Reson Med*. 2014. [Epub ahead of print].
13. Luciani A, Vignaud A, Cavet M, et al. Liver cirrhosis: intravoxel incoherent motion MR imaging–pilot study. *Radiology*. 2008;249:891–899.
14. Moteki T, Horikoshi H. Evaluation of hepatic lesions and hepatic parenchyma using diffusion-weighted echo-planar MR with three values of gradient b-factor. *J Magn Reson Imaging*. 2006;24:637–645.
15. Patel J, Sigmund EE, Rusinek H, et al. Diagnosis of cirrhosis with intravoxel incoherent motion diffusion MRI and dynamic contrast-enhanced MRI alone and in combination: preliminary experience. *J Magn Reson Imaging*. 2010;31:589–600.
16. Pekar J, Moonen CT, van Zijl PC. On the precision of diffusion/perfusion imaging by gradient sensitization. *Magn Reson Med*. 1992;23:122–129.
17. Wirestam R, Borg M, Brockstedt S, et al. Perfusion-related parameters in intravoxel incoherent motion MR imaging compared with CBV and CBF measured by dynamic susceptibility-contrast MR technique. *Acta Radiol*. 2001;42:123–128.
18. Yao L, Sinha U. Imaging the microcirculatory proton fraction of muscle with diffusion-weighted echo-planar imaging. *Acad Radiol*. 2000;7:27–32.
19. Sigmund EE, Vivier PH, Sui D, et al. Intravoxel incoherent motion and diffusion-tensor imaging in renal tissue under hydration and furosemide flow challenges. *Radiology*. 2012;263:758–769.
20. Alison M, Chalouhi GE, Autret G, et al. Use of intravoxel incoherent motion MR imaging to assess placental perfusion in a murine model of placental insufficiency. *Invest Radiol*. 2013;48:17–23.
21. Chandarana H, Lee VS, Hecht E, et al. Comparison of biexponential and monoexponential model of diffusion weighted imaging in evaluation of renal lesions: preliminary experience. *Invest Radiol*. 2011;46:285–291.
22. Ebrahimi B, Rihal N, Woollard JR, et al. Assessment of renal artery stenosis using intravoxel incoherent motion diffusion-weighted magnetic resonance imaging analysis. *Invest Radiol*. 2014;49:640–646.
23. Iima M, Reynaud O, Tsurugizawa T, et al. Characterization of glioma microcirculation and tissue features using intravoxel incoherent motion magnetic resonance imaging in a rat brain model. *Invest Radiol*. 2014;49:485–490.
24. Lemke A, Stieltjes B, Schad LR, et al. Toward an optimal distribution of *b* values for intravoxel incoherent motion imaging. *Magn Reson Imaging*. 2011;29:766–776.
25. Lu Y, Jansen JF, Mazaheri Y, et al. Extension of the intravoxel incoherent motion model to non-Gaussian diffusion in head and neck cancer. *J Magn Reson Imaging*. 2012;36:1088–1096.
26. Bourne RM, Panagiotaki E, Bongers A, et al. Information theoretic ranking of four models of diffusion attenuation in fresh and fixed prostate tissue ex vivo. *Magn Reson Med*. 2014;72:1418–1426.
27. Quentin M, Blondin D, Klasen J, et al. Comparison of different mathematical models of diffusion-weighted prostate MR imaging. *Magn Reson Imaging*. 2012;30:1468–1474.
28. Yuan J, Yeung DK, Mok GS, et al. Non-Gaussian analysis of diffusion weighted imaging in head and neck at 3 T: a pilot study in patients with nasopharyngeal carcinoma. *PLoS One*. 2014;9:e87024.
29. Jansen JF, Stambuk HE, Koutcher JA, et al. Non-Gaussian analysis of diffusion-weighted MR imaging in head and neck squamous cell carcinoma: a feasibility study. *AJNR Am J Neuroradiol*. 2010;31:741–748.
30. Lu H, Jensen JH, Ramani A, et al. Three-dimensional characterization of non-Gaussianwater diffusion in humans using diffusion kurtosis imaging. *NMR Biomed*. 2006;19:236–247.
31. Filli L, Wurnig M, Nanz D, et al. Whole-body diffusion kurtosis imaging: initial experience on non-Gaussian diffusion in various organs. *Invest Radiol*. 2014;49:773–778.
32. Kuder TA, Stieltjes B, Bachert P, et al. Advanced fit of the diffusion kurtosis tensor by directional weighting and regularization. *Magn Reson Med*. 2012;67:1401–1411.
33. Roethke MC, Kuder TA, Kuru TH, et al. Evaluation of diffusion kurtosis imaging versus standard diffusion imaging for detection and grading of peripheral zone prostate cancer. *Invest Radiol*. 2015;50:483–489.
34. Huang Y, Chen X, Zhang Z, et al. MRI quantification of non-Gaussian water diffusion in normal human kidney: a diffusional kurtosis imaging study. *NMR Biomed*. 2015;28:154–161.
35. Pentang G, Lanzman RS, Heusch P, et al. Diffusion kurtosis imaging of the human kidney: a feasibility study. *Magn Reson Imaging*. 2014;32:413–420.